Resolving the Regional Signature of the Annular Modes

PAUL J. KUSHNER AND GABRIEL LEE

Department of Physics, University of Toronto, Toronto, Ontario, Canada

(Manuscript received 4 October 2005, in final form 27 June 2006)

ABSTRACT

A sector EOF analysis applied to the extratropical tropospheric circulation extracts robust circulation patterns that represent the regional signature of the annular modes. These regional patterns are eastward-propagating, long baroclinic wave structures with the dipolar meridional structure in the streamflow of the annular modes. The regional dipole patterns are also connected to the annular modes through their temporal correlation and their eddy flux signatures. These results serve to relate the hemispheric and the regional perspectives on the annular modes.

1. Introduction

In this study, we pursue the ongoing question of the zonal structure of the annular modes. The annular modes (AMs) are usually defined as the first EOF of the hemisphere-wide streamflow in the Northern Hemisphere (NH) or Southern Hemisphere (SH) extratropics (Thompson and Wallace 1998, 2000). The hemisphere-wide EOF analysis produces hemispheric-scale streamflow patterns with a dipolar meridional structure and relatively little zonal structure. On the other hand, teleconnection analysis or EOF analysis on zonally limited extratropical sectors produces regional-scale streamflow patterns, like the North Atlantic Oscillation (NAO), with the hemispheric AMs' dipole meridional structure but with a localized zonal structure (Deser 2000; Ambaum et al. 2001; Cohen and Saito 2002; Cash et al. 2002, 2005; Vallis et al. 2004). Thus, the AMs' meridional structure appears to be robust but their zonal structure depends on the analysis technique and so is not as robust. This leads to the question of whether the hemispheric-scale pattern is physically meaningful or a mere statistical artifact (e.g., Robinson 2004; Cash et al. 2004; Watanabe 2005; Cash et al 2007). A clear answer to this question will allow us to better understand the AMs' role in climate variability and climate change (e.g., Thompson and Wallace 1998; Thompson and Solomon 2002).

Here we systematically examine how the EOFs of the extratropical tropospheric streamflow depend on the zonal width $\delta\lambda$ of the analysis region (section 2), and find results that at least partially reconcile the hemispheric- and regional-scale views of the AMs (sections 3–5). The standard hemispheric (Thompson–Wallace) definition of the AMs corresponds to $\delta\lambda = 360°$, whereas regional sector analyses that give rise to the NAO and the sector EOF patterns of Cohen and Saito (2002) and Cash et al. (2002, 2005) correspond to sector widths $\delta\lambda = 90°–120°$. We show that regional AM signatures emerge for smaller analysis sector widths, and even for an analysis domain that includes only a single longitude. For narrow sectors the AM signatures are no longer the dominant pattern of variability, but the narrow sector analysis produces a more sharply resolved picture of the AM regional structure than the wider sector analysis. The regional signatures take the form of long baroclinic wave structures (section 3c) and so provide a novel view of how the AM might be generated. Although results in the Southern Hemisphere (section 3) are simpler than in the Northern Hemisphere (section 4), the regional signatures are similar in both hemispheres. The analysis opens several research questions that we discuss in the conclusions (section 5).

2. Method

We are looking for a robust regional signature of the AMs in the extratropical troposphere. Baldwin (2001)

Corresponding author address: Dr. Paul J. Kushner, Dept. of Physics, University of Toronto, 60 St. George St., Toronto, ON M5S 1A7, Canada.
E-mail: paul.kushner@utoronto.ca

DOI: 10.1175/JCLI4106.1

shows that the tropospheric signatures of the hemispheric AMs are robust: we see essentially the same spatial structures whether NH or SH data are used, whether zonally averaged or zonally unaveraged data are used, and whether winter season monthly data or year-round daily data are used. In the same vein, we seek regional tropospheric AM signatures that occur in both hemispheres, in all seasons, and, in addition, in all zonal sectors.

Following Baldwin (2001) we use the daily extratropical surface pressure field $p_s(\lambda, \phi, t)$ from the 1979–2004 National Centers for Environmental Prediction–National Center for Atmospheric Research (NCEP–NCAR) reanalysis and retain all days except for leap days. (When we instead use the 1993–2004 period we find no substantial change in the results we report.) Here, λ denotes longitude, ϕ denotes latitude, and t denotes time. We multiply $p_s(\lambda, \phi, t)$ by $\sqrt{\cos\phi}$ at each λ and t and then remove a climatology that has been smoothed with a 31-day running mean filter from the result. We denote the resulting surface pressure anomaly field by $\tilde{p}_s(\lambda, \phi, t)$.

We carry out a sequence of EOF analyses on the zonal mean of $\tilde{p}_s(\lambda, \phi, t)$ in extratropical sectors with zonal boundaries $\lambda_c \pm \delta\lambda/2$ and meridional boundaries (as in Baldwin 2001) 90° and 22.5° latitude. We perform separate calculations for the SH (see section 3) and the NH (see section 4). We denote the sector zonal mean of $\tilde{p}_s(\lambda, \phi, t)$ by $\overline{p}_s(\phi, t; \delta\lambda, \lambda_c)$; the notation $\overline{p}_s(\phi, t; \delta\lambda, \lambda_c)$ distinguishes the local dependence on the coordinates ϕ and t from the nonlocal dependence on the sector parameters $\delta\lambda$ and λ_c. Figure 1 illustrates two SH sectors, one with ($\delta\lambda = 180°$, $\lambda_c = 90°\text{W} = 270°$) and another with ($\delta\lambda = 20°$, $\lambda_c = 150°$). We calculate $\overline{p}_s(\phi, t; \delta\lambda, \lambda_c)$ for

$$\lambda_c = \{0°, 10°, \ldots, 350°\}, \quad \text{and} \tag{1}$$

$$\delta\lambda = \{0°, 5°, 10°, 15°, 20°, 30°, \ldots, 170°, 180°, 200°, 220°, \ldots, 360°\}. \tag{2}$$

In our notation $\overline{p}_s(\phi, t; \delta\lambda = 360°, \lambda_c) = \overline{p}_s(\phi, t; \delta\lambda = 360°)$ corresponds to the standard zonal mean of $\tilde{p}_s$ (which is independent of λ_c), and $\overline{p}_s(\phi, t; \delta\lambda = 0°, \lambda_c) = \tilde{p}_s(\lambda_c, \phi, t)$ corresponds to taking $\tilde{p}_s$ at the single longitude λ_c. The single longitude $\delta\lambda = 0°$ notation is understood to imply that we are sampling the data at the smallest applicable zonal grid scale, which is 2.5° for the NCEP–NCAR reanalysis.

In both the NH and SH, we carry out a separate principal component analysis for each $\delta\lambda$ and λ_c. From this we obtain a set of unit amplitude EOFs $\upsilon_i(\phi; \delta\lambda, \lambda_c)$, associated unit amplitude principal component (PC) time series $u_i(t; \delta\lambda, \lambda_c)$, and eigenvalues $\Lambda_i(\delta\lambda, \lambda_c)$. Here the index i indicates the rank of the EOF. The calculations are carried out using MATLAB's singular value decomposition routine on the $\overline{p}_s(\phi, t; \delta\lambda, \lambda_c)$. We stress that each EOF $\upsilon_i(\phi; \delta\lambda, \lambda_c)$ is a unit amplitude quantity that depends explictly on latitude alone. These are distinct from the regression maps that we will describe below and that can depend on longitude and height in addition to latitude.

Figure 1 plots the SH first EOFs $\upsilon_1(\phi; \delta\lambda = 180°, \lambda_c = 270°)$ and $\upsilon_1(\phi; \delta\lambda = 20°, \lambda_c = 150°)$ for the analysis sectors mentioned above (see caption for sign convention and other details). Notice that the first EOF for the narrower sector is monopolar and for the wider sector is dipolar; we will see in section 3a that this behavior carries over more generally.

We define the "λ_c mean" to be the average over center longitudes λ_c; this represents a kind of ensemble average over all sectors. We denote the λ_c mean of any function $f(\lambda_c)$ by $[f]_{\lambda_c}$. Thus, for example, the λ_c mean of the ith EOFs $\upsilon_i(\phi; \delta\lambda, \lambda_c)$ is $[\upsilon_i(\phi; \delta\lambda)]_{\lambda_c}$ and can be regarded as a function of ϕ and $\delta\lambda$ (see, e.g., Figs. 3a–c).

We also calculate "λ_c-mean regression maps" that depict how various fields vary coherently with a given PC time series $u_i(t; \delta\lambda, \lambda_c)$. For example, to calculate the λ_c-mean regression map for p_s with the first EOF PC time series $u_1(t; \delta\lambda = 100°, \lambda_c)$ (see Fig. 4a), we first calculate the regression (i.e., the temporal covariance) between $p_s(\lambda, \phi, t)$ and each of the 36 $u_1(t; \delta\lambda = 100°, \lambda_c)$ [i.e., one for each of the 36 λ_c values in Eq. (1)]. The u_i are unit amplitude, so these maps each represent the variation in surface pressure per unit standard deviation of the PC time series. These maps are then shifted in longitude λ so that they share a common sector center λ_c, which we choose for plotting purposes to be the date line $\lambda_c = 180°$; finally, we take the λ_c mean of these shifted maps to produce the plot. Because of the shifting to the date line, the center longitude of the plot is arbitrary; geographic boundaries are included for reference only.

3. Results: Southern Hemisphere

a. *Sensivity of EOF structure to* $\delta\lambda$

Our key results concern how the meridional structure of the EOFs of the extratropical streamflow depends on the analysis sector width $\delta\lambda$. By construction we know that as $\delta\lambda \to 360°$ the EOFs $\upsilon_i(\phi; t; \delta\lambda, \lambda_c)$ become independent of λ_c because the sector zonal mean field $\overline{p}_s(\phi, t; \delta\lambda, \lambda_c)$ becomes independent of λ_c. We also know that for $\delta\lambda = 360°$ the first SH EOF is exactly the Baldwin (2001) Southern Annular Mode (SAM) definition based on the daily (and all year) zonal-mean

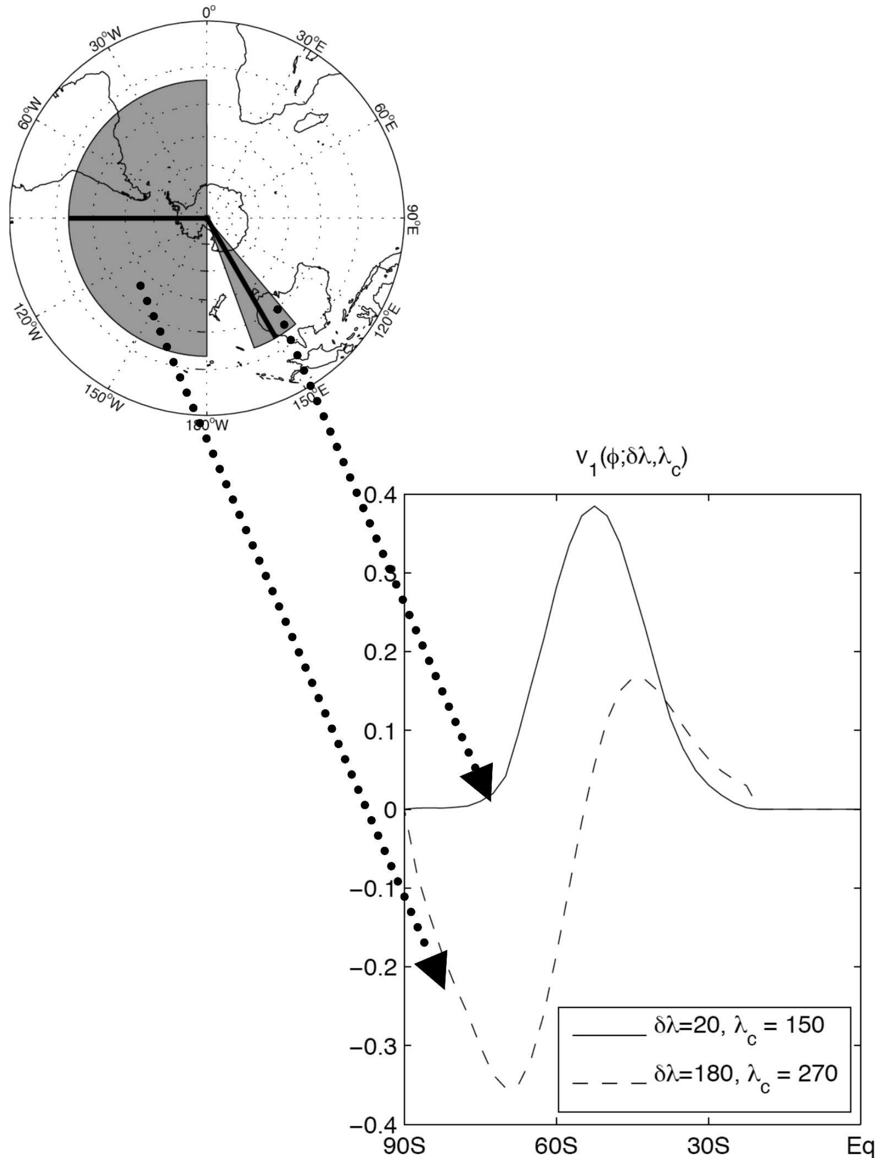

FIG. 1. The shaded regions in the polar stereographic map shows two representative SH sectors for the EOF analysis. The dotted arrows point from the analysis sectors to the corresponding first EOFs in the line plot. The solid curve in the line plot is the first EOF $\upsilon_1(\phi; \delta\lambda = 20°, \lambda_c = 150°)$ and the dashed curve is the first EOF $\upsilon_1(\phi; \delta\lambda = 180°, \lambda_c = 270°)$. In this and the subsequent figures, the EOFs are chosen so that the monopolar EOF maximum is positive and so that the dipolar EOF is consistent with the positive phase of the SAM as conventionally defined. The magnitude of the υ_i is determined by the fact that the sum of the squares of each υ_i over latitude points is unity. We note that each υ_i is zero equatorward of 22.5° latitude.

surface pressure $\overline{p}_s(\phi, t; \delta\lambda, = 360°)$.[1] But, as we will now show, the meridional AM structure emerges at considerably narrower sector widths $\delta\lambda$.

Figure 2 plots the first EOFs $\upsilon_1(\phi; \delta\lambda, \lambda_c)$ for $\delta\lambda = \{0°, 70°, 100°\}$. As explained in the caption, the longitude dependence in the plot reflects the dependence of the meridional structure of the υ_1 on the sector center λ_c. For the single-longitude calculation with $\delta\lambda = 0°$ (Fig. 2a) the $\upsilon_1(\phi; \delta\lambda = 0°, \lambda_c)$ are monopolar, similar to the narrow sector EOF (solid curve) in Fig. 1. For the wide sector calculation with $\delta\lambda = 100°$ (Fig. 2c), the

[1] We have verified that the first EOF $\upsilon_1(\phi; \delta\lambda = 360°)$ qualitatively reproduces the results of Baldwin for his analysis period (not shown). The values for variance explained by each EOF are somewhat larger in our analysis.

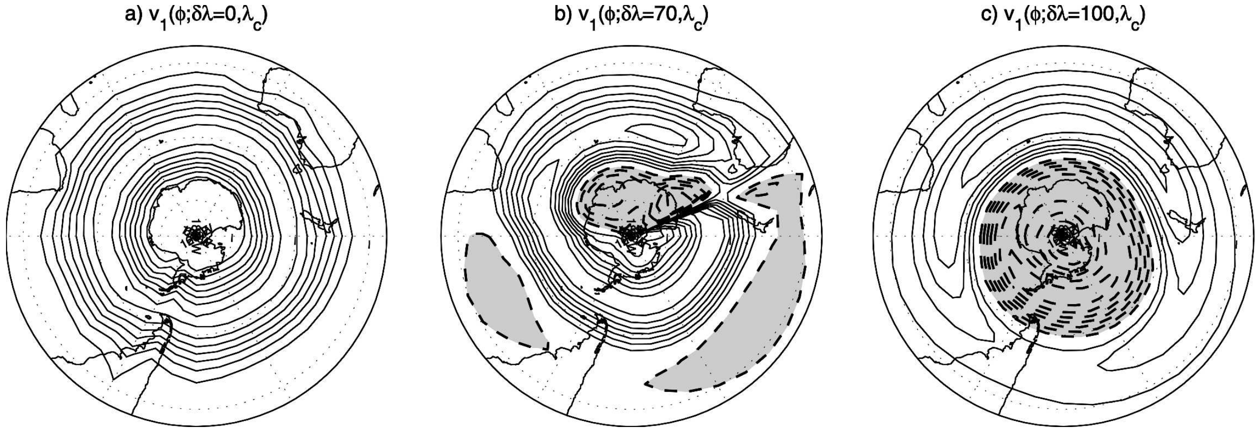

FIG. 2. The first SH EOF $\upsilon_1(\phi;\,\delta\lambda,\,\lambda_c)$ for (a) $\delta\lambda = 0°$, (b) $\delta\lambda = 70°$, and (c) $\delta\lambda = 100°$. Each contour plot shows, for a given $\delta\lambda$, the set of unit amplitude latitude-dependent υ_1 for each of the 36 sector centers $\lambda_c = \{0°, 10°, \ldots, 350°\}$. The contour interval is 0.05 and the negative contours are dashed and shaded. The discontinuity in the contour lines in (b) reflects the application of the sign convention described in the caption for Fig. 1.

$\upsilon_1(\phi;\,\delta\lambda = 100°,\,\lambda_c)$ are dipolar in most sectors, similar to the wider sector EOF (dashed curve) in Fig. 1. For the intermediate-width sectors with $\delta\lambda = 70°$ (Fig. 2b), the $\upsilon_1(\phi;\,\delta\lambda = 70°,\,\lambda_c)$ are not robust from sector to sector: they are monopolar for some λ_c and dipolar for other λ_c.

We now show more systematically how the first EOFs depend on sector width $\delta\lambda$. Figure 3a plots as a function of ϕ and $\delta\lambda$ the λ_c-mean first EOF $[\upsilon_1(\phi;\,\delta\lambda)]_{\lambda_c}$. (See section 2 for the definition of the λ_c mean.) As Figs. 1–2 imply, for narrower sectors ($0° < \delta\lambda < 50°$), the λ_c-mean pattern $[\upsilon_1(\phi;\,\delta\lambda)]_{\lambda_c}$ is monopolar; for wider sectors ($90° < \delta\lambda < 360°$), the λ_c-mean pattern $[\upsilon_1(\phi;\,\delta\lambda)]_{\lambda_c}$ is dipolar. The range $50° < \delta\lambda < 90°$ involves a transition between the two patterns in which the structures are not robust from one sector to another.

Our first key result follows from Fig. 3b, which plots $[\upsilon_2(\phi;\,\delta\lambda)]_{\lambda_c}$, that is, the λ_c-mean second EOF. Even though $\delta\lambda = 90°$ represents the lower bound at which the dipolar structure dominates the variability (Fig. 3a), the dipolar structure does not disappear for narrower sectors. Instead, the dipolar structure emerges as a secondary pattern of variability for $\delta\lambda < 50°$ in Fig. 3b. At the same time as the dipolar structure switches from the first EOF for $\delta\lambda > 90°$ to the second EOF for $\delta\lambda < 50°$, the monopolar structure switches from the second EOF to the first EOF. By contrast, the λ_c-mean third EOF $[\upsilon_3(\phi;\,\delta\lambda)]_{\lambda_c}$, which we plot in Fig. 3c, remains stable and retains a tripole structure for all $\delta\lambda$.

b. The regional signature of the SAM

We now show that the dipolar second EOF pattern that emerges for small sector widths in Fig. 3b is the regional signature of the SAM: it remains a significant contributor to the variability, it is robust from sector to sector, it has a regional NAO-like structure, and it is directly related to the hemispheric SAM.

We first demonstrate that the dipolar second EOF pattern $[\upsilon_2(\phi;\,\delta\lambda)]_{\lambda_c}$ is a significant contributor to the variability for $\delta\lambda < 50°$. Figure 3d plots the λ_c-mean variance fraction accounted for by EOFs 1–3 as a function of $\delta\lambda$ (i.e., $[\Lambda_j/\Sigma_i\Lambda_i]_{\lambda_c}$ for $j = 1, 2, 3$ in our notation). The variance fraction for the $\upsilon_2(\phi;\,\delta\lambda = 0°,\,\lambda_c)$ is about 28%, which represents a significant portion of the variability compared to the variance fraction for the first EOF $\upsilon_1(\phi;\,\delta\lambda = 0°,\,\lambda_c)$, which is approximately 46%. For the third EOF $\upsilon_3(\phi;\,\delta\lambda = 0°,\,\lambda_c)$, the variance fraction is about 10%.

Next, we show that the narrow sector second EOF dipolar patterns $\upsilon_2(\phi;\,\delta\lambda,\,\lambda_c)$ are robust in the sense that they are similar in all the sectors. Figure 3e plots a relative measure of this robustness, namely the squared amplitude of the λ_c-mean EOFs as a function of $\delta\lambda$; call this quantity "R." Because the υ_i are unit amplitude, when the EOFs depend weakly on λ_c [as for $\upsilon_1(\phi;\,\delta\lambda = 0°,\,\lambda_c)$ in Fig. 2a], R will be less than but close to unity; when the EOFs depend strongly on λ_c [as for $\upsilon_1(\phi;\,\delta\lambda = 70,\,\lambda_c)$ in Fig. 2], R will be positive but relatively small.[2] By construction, as we see in Fig. 3e, $R \to 1$ for all EOFs as $\delta\lambda \to 360°$. But Fig. 3e also shows that for

[2] Here $R \geq 0$ if we choose the polarity of the EOFs so that the dot product of any pair of EOFs is positive semidefinite. We can calculate R in the following simple example: suppose the EOFs are in pattern a for half of the sectors and in pattern b for the other half, and that a and b are orthogonal with $ab = 0$, where the dot product is the sum over latitude points of the products of the vector components. In this case $R = [(a + b)(a + b)]/4 = 1/2$.

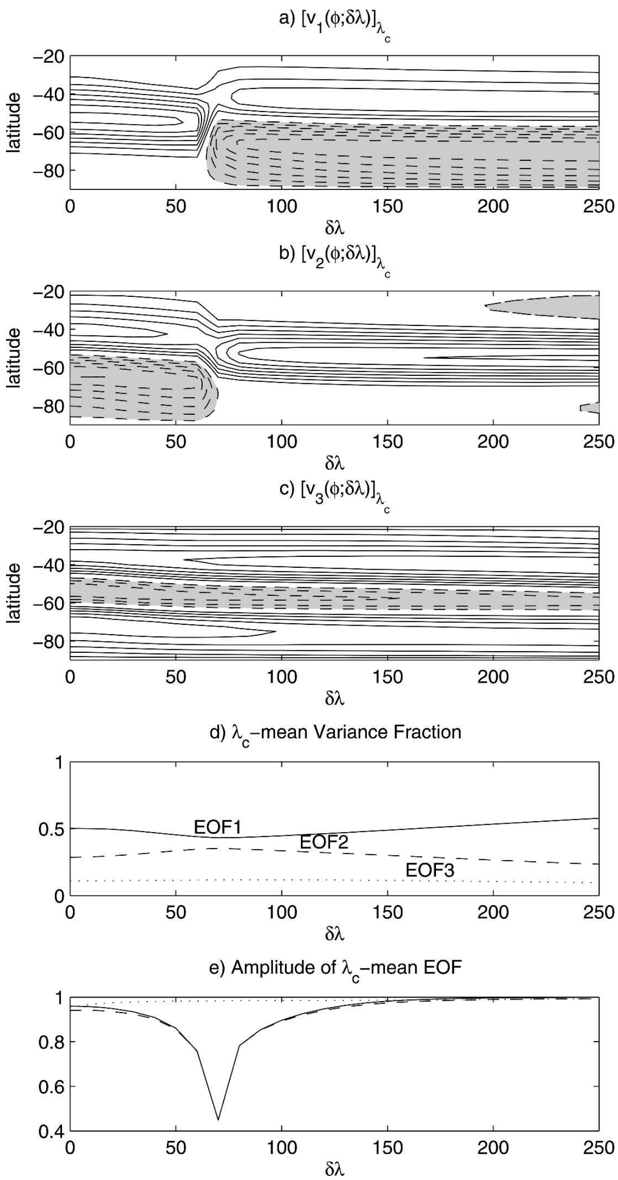

FIG. 3. (a) The λ_c-mean first SH EOF $[\upsilon_2(\phi;\ \delta\lambda)]_{\lambda_c}$ as a function of latitude and sector width $\delta\lambda$. The contour interval is 0.05 and the negative contours are dashed. (b) Same as in (a), but for $[\upsilon_2(\phi;\ \delta\lambda)]_{\lambda_c}$. (c) Same as in (a), but for $[\upsilon_3(\phi;\ \delta\lambda)]_{\lambda_c}$. (d) The λ_c-mean variance fraction for υ_1 (solid), υ_2 (dashed), and υ_3 (dotted). (e) Same as in (d), but for R, which is the squared amplitude of the λ_c-mean EOF.

the three leading EOFs, and in particular for the dipolar EOF, $R > 0.8$ for $\delta\lambda < 50°$ and that R is almost unity for $\delta\lambda = 0°$. The lack of robustness seen in the relatively small R values in the range $50° < \delta\lambda < 90°$ is expected from Figs. 2 and 3a,b. For the third EOF $\upsilon_3(\phi;\ \delta\lambda,\ \lambda_c)$, R remains near unity for all $\delta\lambda$, which is not surprising given that this EOF appears to be independent of the sector width (Fig. 3c).

Figure 3 shows that a robust and significant meridional dipolar pattern remains as the second EOF as $\delta\lambda$ is decreased below 90°. We now ask how the zonal structure associated with the dipole EOFs depends on $\delta\lambda$. To answer this question, we regress the surface pressure field $p_s(\lambda,\ \phi,\ t)$ on the PC time series corresponding to the dipolar EOFs. Figure 4 plots the λ_c-mean regression (section 2) of p_s with $u_1(t;\ \delta\lambda = 100°)$ (see Fig. 4a) and with $u_2(t;\ \delta\lambda = 0°,\ \lambda_c)$ (see Fig. 4b). For $\delta\lambda > 90°$, the circulation pattern more or less fills the sector, as in Fig. 4a and as seen in the sector EOFs in the simulations of Cash et al. (2002). But as $\delta\lambda$ falls below 90°, a more localized circulation pattern appears, as in Fig. 4b. The zonal details have become better resolved, and the pattern more independent of the sector width.

The localized dipolar pattern in Fig. 4a, which we interpret as the regional circulation signature of the SAM, can be obtained independently of a particular EOF analysis by using an index based on the difference in surface pressure between two locations (e.g., Wallace 2000; Gong and Wang 1999; Gerber 2006). In this case, we define a local dipole index $\Delta p_s(\lambda_c,\ t) = p_s(\lambda_c,\ \phi = 40°\text{S},\ t) - p_s(\lambda_c,\ \phi = 65°\text{S},\ t)$, that represents the difference in surface pressure between 40° and 65°S at each longitude λ_c. The latitudes 65° and 40°S correspond to the typical centers of action of the dipolar $\delta\lambda = 0°$ EOF and are the latitudes used by Gong and Wang (1999) in their definition of the SAM. The correlation between the time series and the corresponding PC time series $u_1(t,\ \delta\lambda = 0°,\ \lambda_c)$ is very high (greater than 0.95) everywhere except in the vicinity of South America, and the λ_c mean of this correlation is 0.93. Thus the pressure difference index $\Delta p_s(\lambda_c,\ t)$ and the regional dipole PC time series $u_1(t,\ \delta\lambda = 0°,\ \lambda_c)$ are essentially equivalent.

In Figs. 3a,b, we see that the meridional dipolar structure slowly shifts poleward as $\delta\lambda$ is increased. Figure 4 helps explain this poleward shift: notice in Fig. 4b that the meridional location of the maxima at each longitude curve poleward away from the center longitude (the date line in the plot). In the sector zonal mean, as $\delta\lambda$ is increased and wider zonal sectors are sampled, these higher-latitude contributions become more pronounced, resulting in the poleward shift of the dipole.

We have tried to make clear the connection in spatial structure between the narrow sector, wide sector, and hemispheric dipole patterns. We can also connect the temporal variability of these patterns. For example Fig. 5 plots the temporal correlation between the hemispheric SAM index $u_1(t;\ \delta\lambda = 360°)$ and the $\delta\lambda = 0°$ dipolar EOF time series $u_2(t;\ \delta\lambda = 0°,\ \lambda_c)$, as a function

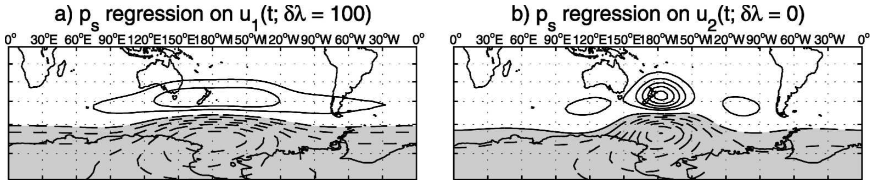

FIG. 4. (a) The λ_c-mean regression map for p_s on $u_2(t;\ \delta\lambda = 0°,\ \lambda_c)$, averaged over λ_c. The contour interval (CI) is 1 hPa and the negative contours are dashed and shaded. The date line is chosen arbitrarily as a reference point for plotting purposes. (b) Same as in (a), but for $\delta\lambda = 100°$.

of center longitude λ_c. The correlation remains very significant (between 0.37 and 0.57, with a mean of 0.48) for all longitudes.[3] Thus, for example, positive SAM days are typically related to positive phases of the regional dipole pattern $[\upsilon_2(\phi;\ \delta\lambda = 0°)]_{\lambda_c}$.

We can explain the approximately 0.5 correlation in Fig. 5 in terms of the working hypothesis (Wallace 2000; Cash et al. 2002, 2005) that the hemispheric AM represents a superposition of regional dipole events. As a simple model, suppose (see, e.g., Cohen and Saito 2002; Gerber and Vallis 2005) that we have a set of N independent and identically distributed regional dipole PC time series, each corresponding to a dipole pattern of zonal width $\Delta\lambda = 360°/N$. The time series are independent and so are mutually uncorrelated. We generate a hemispheric AM index by taking the arithmetic mean of the regional dipole PC time series (this would correspond to a zonal mean). The correlation between the hemispheric AM and each of the regional dipole PC time series is $1/\sqrt{N} = \sqrt{\Delta\lambda/360°}$. For the correlation of 0.5 from Fig. 5, we would have $\Delta\lambda \approx 90°$, which is in qualitative agreement with the zonal scale of the pattern in Fig. 4b.

The AMs (the dipole patterns for $\delta\lambda = 360°$) have strong signatures in the extratropical eddy fluxes of heat and momentum, as summarized by their signature in Eliassen–Palm fluxes (e.g., Limpasuvan and Hartmann 2000; Lorenz and Hartmann 2001). These signatures provide the foundation for theories of AM variability that involve feedbacks between the transient baroclinic eddy forcing and the zonal mean flow (e.g., Robinson 2000; Lorenz and Hartmann 2001; Rashid and Simmonds 2004). We find, somewhat unexpectedly, that these signatures in the eddy flux fields are also associated with the regional dipole events, and not just hemispheric AM events. Figure 6 demonstrates an example of this; to describe it requires some additional notation. Let $\langle A \rangle$ represent the regression of some field A with a particular PC time series, and let $\overline{B}$ and $B^* = B - \overline{B}$ denote the zonal mean and zonally asymmetric ("eddy") components of some field B. In this notation, $\langle \overline{\upsilon^* T^*} \rangle$, which depends on latitude and height, is the regression of the daily time series of the zonal mean eddy heat flux $\overline{\upsilon^* T^*}$ with a PC time series. Figure 6a plots $\langle \overline{\upsilon^* T^*} \rangle$ for the hemispheric SAM PC time series $u_1(t;\ \delta\lambda = 360°)$. This is the flux anomaly associated with a "1σ" SAM event and is typically dominated by contributions from synoptic-scale transient eddies (Lorenz and Hartmann 2001). On positive SAM days, the poleward transport of heat by synoptic eddies is enhanced in the extratropical troposphere, and on negative SAM days it is attenuated.

Figure 6b plots the λ_c mean of $\langle \overline{\upsilon^* T^*} \rangle$ for the regression of the zonal-mean meridional eddy heat flux and the 36 $u_2(t;\ \delta\lambda = 0°,\ \lambda_c)$ time series. The plot thus represents the signature in the meridional eddy heat flux of a 1σ regional dipole event. The heat flux signatures in Figs. 6a,b are nearly identical, with the hemi-

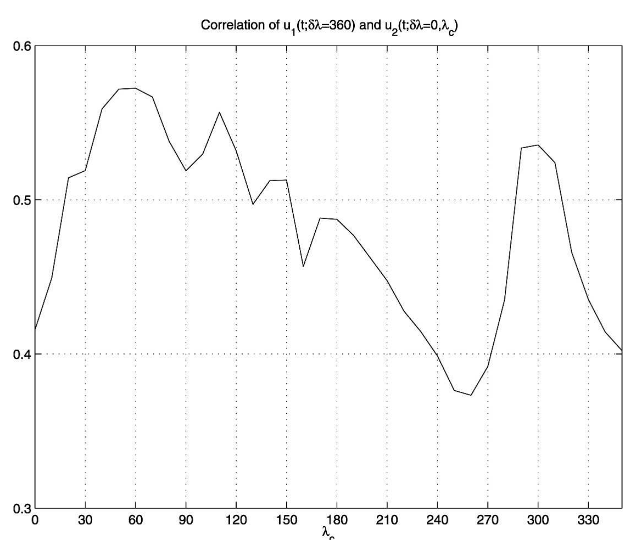

FIG. 5. The temporal correlation between $u_1(t;\ \delta\lambda = 360°)$ and $u_2(t;\ \delta\lambda = 0°,\ \lambda_c)$ as a function of λ_c.

[3] For 26 yr of daily data, there are over 900 separate 10-day periods. Taking 900 as an estimate for the number of degrees of freedom, any correlation above 0.1 would be highly significant.

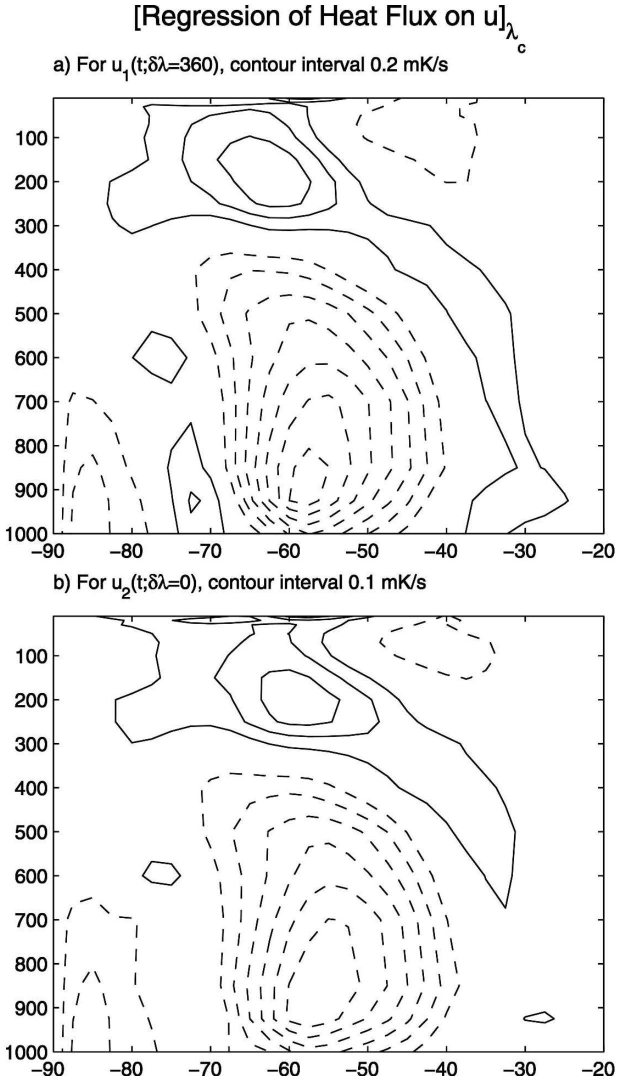

FIG. 6. (a) The regression of the zonal-mean meridional eddy heat flux on $u_1(t;\, \delta\lambda = 360°)$. The CI is 0.2 mK s^{-1} and negative contours are dashed and shaded. (b) The λ_c mean of the regression of the zonal-mean meridional eddy heat flux on $u_2(t;\, \delta\lambda = 0°, \lambda_c)$. The contour interval is 0.1 mK s^{-1} and negative contours are dashed and shaded.

spheric SAM regression pattern having an amplitude of about half that of the regional pattern regression. This suggests that the dynamics that couple the synoptic eddy fluxes and the dipole circulation anomalies might occur on a regional scale. A more complete discussion of the eddy mean–flow interaction aspects is beyond the scope of this study. In section 3c, we will return to the question of why the regional dipole pattern's heat flux signature is half that of the hemispheric AM.

To summarize, we have found that the hemispheric SAM has an NAO-like regional signature with a zonal scale of about 90° longitude. The regional dipolar patterns do not dominate the variability at these scales. Instead, the variability is dominated by the $\delta\lambda = 0°$ monopolar EOFs, whose λ_c-mean circulation signature in p_s is shown in Fig. 7. But the dipole patterns are robust and connected via their spatial structure, temporal correlation, and eddy flux signatures to the SAM pattern, which is the dominant pattern at larger zonal scales. So it appears to be worthwhile to study these "building blocks" of the AMs in more detail.

c. *Some dynamical features of the regional dipole patterns*

We find it instructive to compare the dynamical features of the regional dipole patterns (Fig. 4b) to the regional monopole patterns (Fig. 7). Figures 8a,b plot the λ_c-mean lag correlation for the $u_1(t;\, \delta\lambda = 0°, \lambda_c)$ and $u_2(t;\, \delta\lambda = 0°, \lambda_c)$ time series, as a function of zonal displacement from λ_c and time lag. To obtain Fig. 8a, for example, we choose a base center longitude λ_c, lag correlate $u_1(t;\, \delta\lambda = 0°, \lambda_c)$ with all the $u_1(t;\, \delta\lambda = 0°, \lambda_{c'})$, translate these in λ to obtain a dependence on $\lambda_c - \lambda_{c'}$, and take the λ_c mean.[4]

Figure 8a shows that the monopolar pattern propagates as a zonal wavenumber-3–4 wave packet with phase velocity of about 5° longitude day^{-1} and group velocity of about 30° longitude day^{-1}. The dipole pattern in Fig. 8b, on the other hand, propagates as a weakly dispersive coherent pulse with a phase speed of about 8°–10° day^{-1}. Figure 8 also shows that the monopole patterns are less persistent for a given $\lambda_c - \lambda_{c'}$: the decorrelation time scale for the monopolar pattern is about 2 days and for the dipolar pattern is about 4 days, and significant (>0.1) correlations in the dipole pattern extend past ± 10 days. The overall behavior is qualitatively consistent with the expectation—from barotropic dynamics—that zonally elongated structures like the dipole pattern are of lower frequency and have a slower zonal group speed than more isotropic structures like the monopole pattern (e.g., Hoskins et al. 1983).

The decorrelation times of the regional patterns is short compared to that of the hemispheric AMs: we find that the decorrelation time of the SAM index $u_1(t;\, \delta\lambda = 360°)$ is about 8 days, which is about twice that of

[4] Again (see footnote 3), it may be safely assumed that the 0.1 correlation level is highly significant since the plot involves thirty-six 26-yr daily time series. Even though each time series is not independent, we estimate that there are at least 1800 degrees of freedom, assuming independence between 10-day periods and points separated by a zonal distance of 180°.

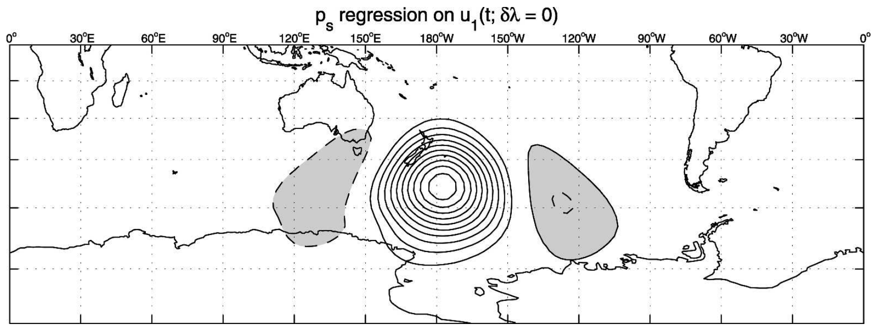

FIG. 7. Same as in Fig. 4b, but for p_s on $u_1(t;\ \delta\lambda = 0°,\ \lambda_c)$: this is the regional monopole pattern.

regional dipole index $u_2(t;\ \delta\lambda = 0°,\ \lambda_c)$ and about 4 times that of the regional monopole index $u_1(t;\ \delta\lambda = 0°,\ \lambda_c)$.[5] The enhanced persistence of the SAM relative to the regional dipole pattern might explain the factor of 2 difference in amplitude between the transient eddy heat flux signatures in Figs. 6a,b: since a SAM event persists longer than an individual regional dipole event, the associated organization of the transient eddy field might be stronger when related to the SAM fluctuations. Consistently, the monopole patterns, which have an even shorter decorrelation time of about 2 days, have a very weak signature in the transient eddy heat flux (not shown) compared to Fig. 6.

One of the unexpected results of our analysis is that both the monopolar and dipolar circulation patterns have a significant baroclinic signature. To show this, we plot in Fig. 9 the λ_c-mean regression with the monopole and dipole PC time series of geopotential height at selected latitudes, as a function of pressure and longitude. For example, Fig. 9a plots the regression with the monopolar EOF PC time series at 52.5°S, which represents the meridional center of action of the $\delta\lambda = 0°$ EOF in Fig. 7. This plot shows the familiar westward phase tilt with height associated with baroclinic wave packets. Lagged regression plots (not shown) show this entire structure moving as a wave group like classical baroclinic wave packets (e.g., Chang 1993), as suggested by Fig. 8a, although these wave structures are larger scale than typical synoptic wave packets.

Figure 9b plots the regression with the dipolar EOF PC time series at 65°S, which represents the poleward center of the dipolar $\delta\lambda = 0°$ EOF in Fig. 4b. A section through the equatorward center at 40°S (not shown) has a similar structure with opposite sign. As was the case for the monopolar pattern, the dipolar pattern has a baroclinic structure, exhibiting a westward tilt with height. Lag regression plots (not shown) also show that this structure moves eastward in the way suggested by Fig. 8b.

The baroclinic structure seen in Fig. 9b leads to our second key result; namely that the regional signature of the AM is a propagating baroclinic wave. To quantify the baroclinic character of the monopolar and dipolar patterns, in Fig. 10 we calculate the meridional heat flux associated with the circulation patterns in Fig. 9. This figure plots the λ_c mean of $\overline{\langle v^*\rangle\langle T^*\rangle}$, that is, the zonal mean of the product of the regressions of the eddy component of the meridional velocity and the eddy component of the temperature. Figure 10 shows that although it is weaker than for the monopolar pattern, the heat flux for the regional dipole pattern is poleward, of significant amplitude, and complementary in structure to that of the monopolar wave packet. In particular the regional dipole heat flux has a significant amplitude near the surface at the meridional centers of action 40° and 65°S. Regional dipole events thus transport a significant amount of heat out of the subtropics and into the high latitudes. The peak magnitude of the heat flux for the monopolar pattern is 0.8 mK s^{-1} and for the dipolar pattern is 0.4 mK s^{-1}; this is comparable to the zonal-mean heat flux signature for North Pacific synoptic baroclinic wave packets (see Fig. 8 of Chang 1993).

We emphasize the distinct physical interpretations that apply to the plot of $\overline{\langle v^*T^*\rangle}$ in Fig. 6b and of $\overline{\langle v^*\rangle\langle T^*\rangle}$ in Fig. 10b. Figure 6b represents a heat flux anomaly whose sign is dependent on the polarity of the regional dipole event: the heat flux anomaly is primarily poleward for the positive phase of the pattern and

[5] This hemispheric AM time scale is somewhat short compared to that of Lorenz and Hartmann (2001), who find a decorrelation time of about 2 weeks, using a tropospheric zonal wind–based definition of the AM. The differences between the zonal wind– and the streamflow-based definitions of the annular mode are not trivial and might account for the discrepancy in time scale (A. Monahan 2006, personal communication).

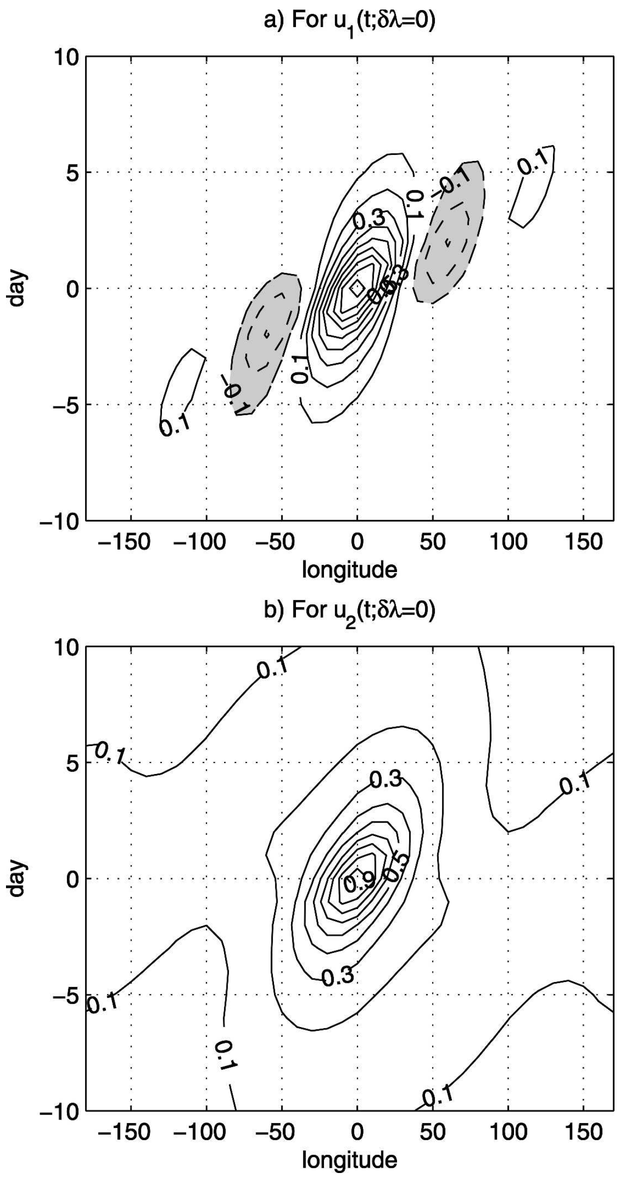

FIG. 8. The λ_c-mean lag correlation of (a) $u_1(t;\, \delta\lambda = 0°,\, \lambda_c)$ and (b) $u_2(t;\, \delta\lambda = 0°,\, \lambda_c)$. The CI is 0.1 and negative contours are dashed and shaded.

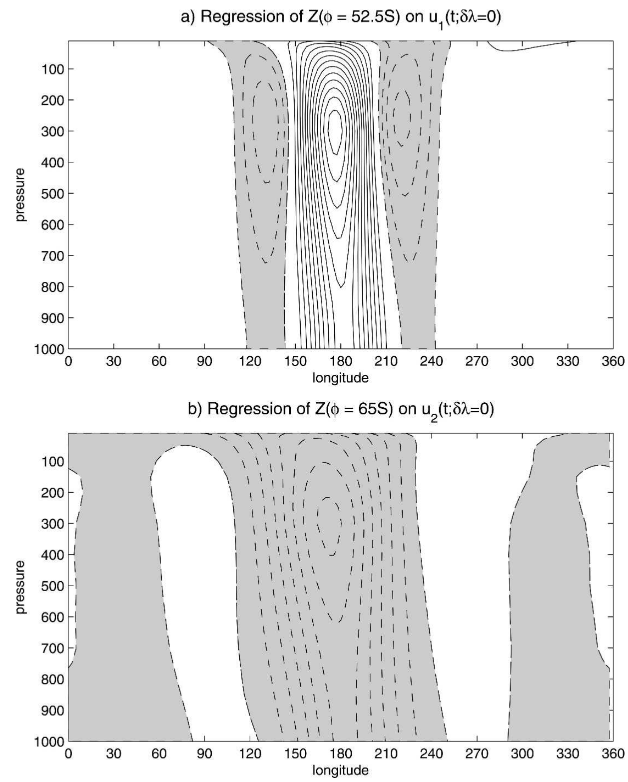

FIG. 9. (a) The λ_c-mean regression of geopotential height at 52.5°S on the monopole index $u_1(t;\, \delta\lambda = 0°,\, \lambda_c)$. The CI is 10 m and the negative contours are dashed and shaded. (b) Same as in (a), but for the geopotential height at 65°S and the dipole index $u_2(t;\, \delta\lambda = 0°,\, \lambda_c)$.

equatorward for the negative phase. Figure 10b, on the other hand, always indicates poleward heat transport (i.e., a westward tilt of geopotential contours with height), whatever the polarity of the regional dipole event. In this way, the propagating dipole pattern is similar to classical baroclinic waves, for which both cyclones and anticyclones transport heat poleward.

We also point out that Fig. 10 depends strongly on the analysis sector width $\delta\lambda$: since the zonal structure of the regression patterns becomes smoother as $\delta\lambda$ increases, the heat flux signature in Fig. 10 will decrease at the same time. By construction, as $\delta\lambda \rightarrow 360°$, this heat flux signature will disappear. Thus, the hemispheric EOF analysis masks the baroclinic character of the regional dynamics.

4. Results: Northern Hemisphere

Although the NH circulation is more zonally asymmetric and has a stronger seasonal cycle than the Southern Hemisphere, Baldwin (2001) has shown that the tropospheric signature of the NAM and SAM, based on daily surface pressure for the entire year, are very similar. We therefore have applied the SH analysis of section 3 to the NH with the idea that the regional dipole patterns might be similar in both hemispheres. The results are summarized as follows:

- The $v_1(\phi;\, \delta\lambda,\, \lambda_c)$ converges to the Baldwin (2001) NAM $[v_1(\phi;\, \delta\lambda = 360°)]$ for sector widths $\delta\lambda > 180°$ (Fig. 11a). This is relatively large compared to the analogous convergence to the SAM in the SH, which occurs for $\delta\lambda > 90°$.

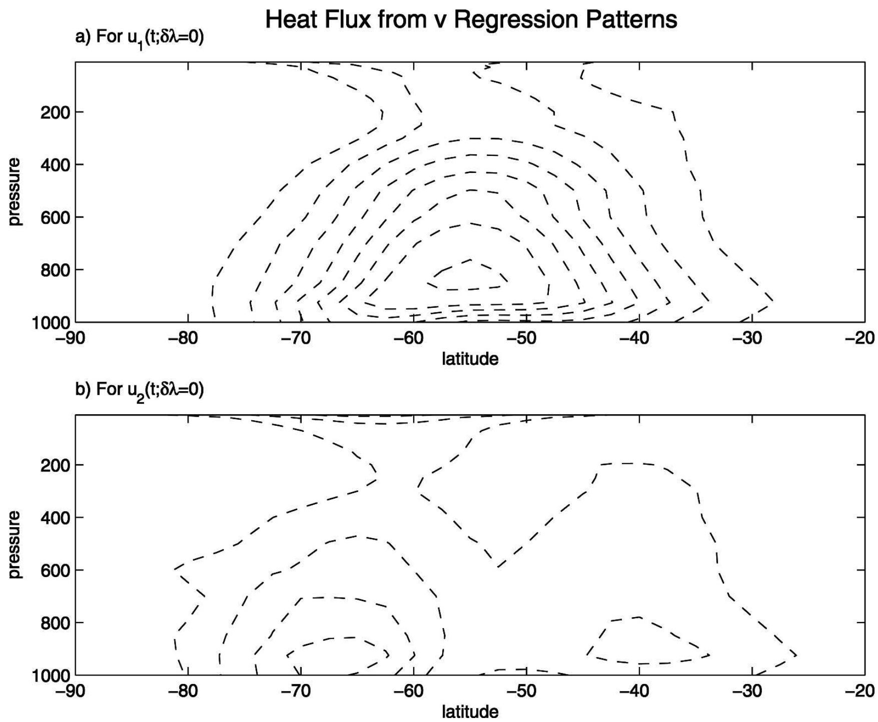

FIG. 10. (a) The λ_c-mean zonal mean eddy meridional heat flux associated with the regression of the meridional wind and the temperature on $u_1(t;\, \delta\lambda = 0°,\, \lambda_c)$. The contour interval is 0.1 mK s^{-1} and the dashed contours are negative. (b) Same as in (a), but for $u_2(t;\, \delta\lambda = 0°,\, \lambda_c)$.

- The switch in the SH case between the monopolar and dipolar first EOF patterns (Figs. 3a,b) does not occur in the NH case (Figs. 11a,b). For example, the two leading EOFs in the NH as $\delta\lambda > 180°$ are both dipolar.
- Nevertheless, for $\delta\lambda < 30°$, a monopolar first EOF and dipolar second EOF emerge with a similar structure to the SH EOFs. These NH regional EOFs are somewhat less robust (more λ_c dependent) than the SH regional EOFs, but explain a comparable portion of the variability (Figs. 11a,b,d,e). Thus, the dipolar NH second EOF, $[\upsilon_2(\phi;\, \delta\lambda = 0°)]_{\lambda_c}$, remains a significant pattern, which we interpret as the regional signature of the NAM.
- The NAO comes out of this analysis as a dominant pattern for the North Atlantic sector, as long as we use a sufficiently wide analysis sector. Figure 12 shows the leading EOF $\upsilon_1(\phi;\, \delta\lambda,\, \lambda_c)$ for $\delta\lambda = \{0°, 30°, 70°, 100°\}$. The first EOF in the limit $\delta\lambda \to 0°$ is monopolar for all λ_c, and the second pattern in this limit is dipolar for all λ_c (not shown), as in the SH. As we expect from the smaller value of the robustness R in Fig. 11e, the details of its structure are more sector dependent than for the SH case in Fig. 2a. As $\delta\lambda$ increases to 30°, 70°, and 100° dipole structures emerge as the dominant patterns first in the North Atlantic sector and then in the North Pacific sector. Figure 12d shows that the dominant EOF remains monopolar over the continents, even for $\delta\lambda = 100°$; this is reminiscent of the regression map of the NAM, as seen in Thompson and Wallace (2000).
- The zonal structure and evolution of the regional signature of the NAM is similar to that of the regional signature of the SAM (e.g., Fig. 13) and exhibits a comparable baroclinic structure (not shown). The correlation between the hemispheric NAM and the regional pattern is somewhat weaker than for the SAM but still quite significant at all longitudes (not shown).

The relatively strong zonal asymmetry and seasonal cycle of the NH extratropical circulation appears to complicate the dependence on $\delta\lambda$ of the EOF structure to a certain extent. But the key results of the SH case carry over to the NH case: the NAM, too, has a regional signature with a baroclinic structure.

5. Conclusions

We repeat our main findings.

1) The regional signature of the annular modes emerges as the second EOF of the extratropical sur-

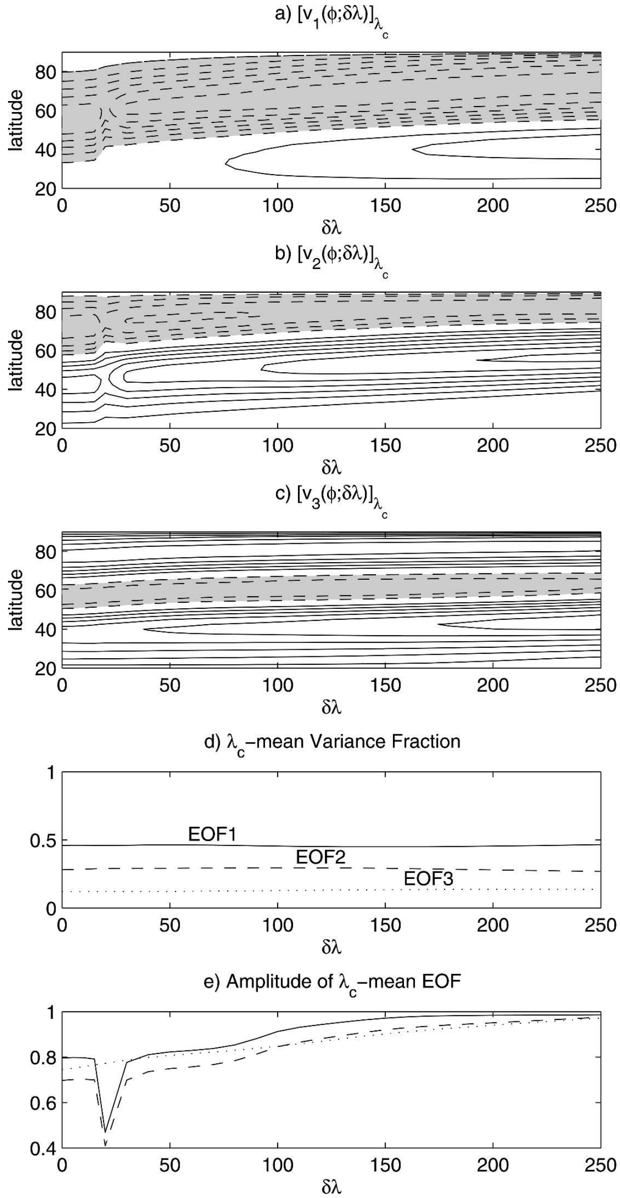

FIG. 11. Same as in Fig. 3, but for the NH. (a) The monopolar pattern that appears as $\delta\lambda \rightarrow 0°$ is plotted with a negative sign, to simplify the contour plot.

face pressure p_s at each longitude—$[\upsilon_2(\phi;\delta\lambda = 0°)]_{\lambda_c}$ in our notation, with time series index $u_2(t; \delta\lambda = 0°, \lambda_c)$ at each longitude λ_c. Although they are not the dominant pattern, these patterns still account for a significant fraction of the variance of the extratropical circulation at each longitude. They are robust in the sense that they occur in both hemispheres, that their meridional structure is similar at all longitudes and that they are found in an analysis that includes all days of the year. They are related through spatial structure, temporal correlations, similarities in frequency distribution, and eddy-forcing quantities to the hemispheric annular modes—$\upsilon_1(\phi; \delta\lambda = 360°)$ in our notation, with time series $u_1(t; \delta\lambda = 360°)$.

2) The regional AM signatures consist of eastward-propagating baroclinic waves of zonal scale of approximately 90° that transport heat poleward in the same manner as classical synoptic-scale baroclinic wave packets. As far as we know, this result has not been previously anticipated: typically, extratropical teleconnection patterns such as the AMs and the NAO are pictured as equivalent barotropic.

Although we have devoted some effort toward examining the detailed dependence of the meridional structure of the EOFs on δλ, the zonal-mean limit $\delta\lambda \rightarrow 360°$ and the single-longitude limit $\delta\lambda \rightarrow 0°$ lead to the most robust and, in our view, the most dynamically interesting results. Nevertheless, the question of why the dipole is the dominant pattern for large δλ but not for small δλ, and of what determines the scale of this transition, are still interesting. We might explain this behavior as a consequence of the tendency for wider sectors to smooth the motion and so bring out lower frequencies. Since lower-frequency eddies tend to be more zonally elongated than higher-frequency eddies (Hoskins et al. 1983), wider sector averages might favor the more persistent zonally elongated patterns. Alternatively, this behavior might relate to the view of Gerber and Vallis (2005) that the dipole hemispheric SAM structures reflect conservation of angular momentum. From this point of view, the $\delta\lambda = 90°$ scale reflects the lower bound for which this angular constraint is important in the SH. In the NH, with its more zonally asymmetric circulation, the dipole NAM structure does not emerge as the dominant mode until $\delta\lambda > 180°$; this may be the relevant zonal scale for the angular momentum constraint in the NH.

One implication of point 2 above might be that the regional dipole patterns, like other baroclinic waves, are self-maintained structures that owe their existence to the background baroclinicity. We might expect that the dipolar baroclinic EOFs correspond to a secondary mode of baroclinic instability with a dipolar meridional structure (seen, e.g., in Simmons and Hoskins 1976; Hartmann 1979; Tanaka and Tokinaga 2002). Hartmann (1979) in particular has shown that the Southern Hemisphere circulation is baroclinically unstable to slowly traveling long waves with a dipolar meridional structure. A baroclinic instability–based theory might provide an explanation for the scale and propagation

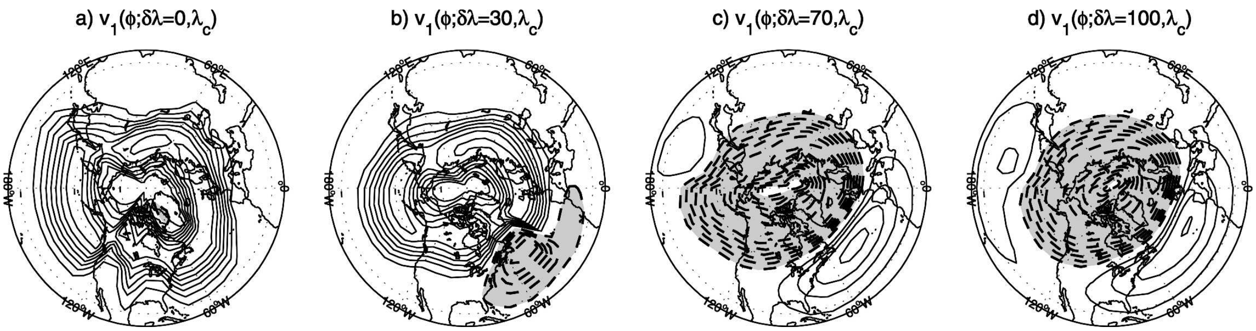

FIG. 12. Same as in Fig. 2, but for the NH and for (a) δλ = 0°, (b) δλ = 30°, (c) δλ = 70°, and (d) δλ = 100° lon.

speed of the regional dipole patterns. Because the growth rates of baroclinic instability typically decrease with decreasing meridional scale, this theory might also account for the relatively weak contribution to the variance of the dipolar baroclinic patterns compared to the monopolar baroclinic patterns. A baroclinic instability–based theory would not explain all the signatures of the AM patterns, for example, the heat flux signature seen in Fig. 6. So it is clear that this theory would complement theories based on regional and zonal eddy mean–flow interactions (e.g., Franzke et al. 2004; Lorenz and Hartmann 2001; Vallis et al. 2004).

We have proposed in section 3b a simple description along the lines of the Gerber and Vallis (2005) model of the AMs in terms of a superposition of independent regional events. To augment this description, we need to build in the propagation characteristics of the regional dipole patterns seen in Fig. 8b, and the possible influence of the zonal mean flow via baroclinic generation of the patterns. This augmented description might explain the fact that significant correlations exist at zero time lag all the way around a latitude circle (Fig. 8b). It might also explain why the annular modes are roughly twice as persistent as the regional dipole patterns (section 3c).

To conclude, we point out that the regional dipole patterns might provide insight into the role of the AMs in stratosphere–troposphere dynamical coupling (e.g., Baldwin and Dunkerton 1999, 2001; Thompson and Wallace 2000; Thompson and Solomon 2002). This coupling is strongly seasonal and so is not handled well within our analysis, which includes all seasons. But Hartmann's (1979) results and the fact that the regional dipole patterns that form the "building blocks" of the annular modes are long baroclinic waves suggest that an investigation of the stratospheric signatures of the regional patterns is well warranted.

Acknowledgments. We thank the Natural Sciences and Engineering Research Council of Canada and the Canadian Foundation for Climate and Atmospheric Sciences for support. Much of this work was completed at the Aspen Center for Physics 2005 Workshop on Novel Approaches to Climate. We also thank Maarten Ambaum (for correcting a mistake in the analysis related to Fig. 5), Edwin Gerber (for the idea of the using the Δp_s index), as well as Adam Monahan, John Fyfe, and the manuscript's reviewers for helpful comments.

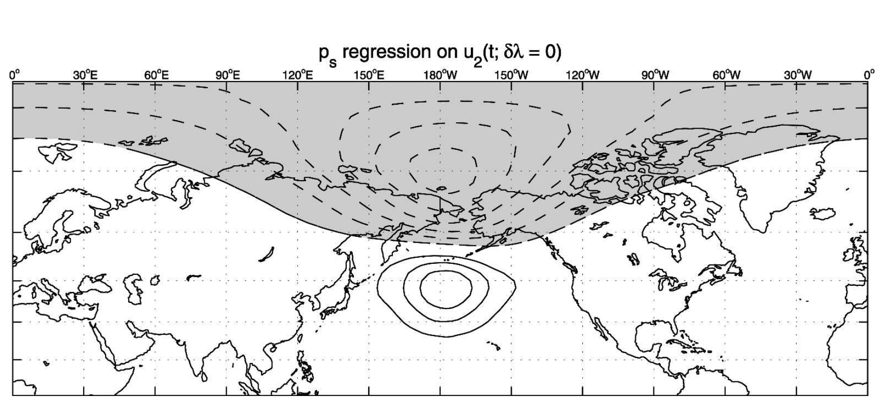

FIG. 13. Same as in Fig. 4b, but for the NH.

REFERENCES

Ambaum, M. H. P., B. J. Hoskins, and D. B. Stephenson, 2001: Arctic Oscillation or North Atlantic Oscillation? *J. Climate,* **14,** 3495–3507.

Baldwin, M., 2001: Annular modes in global daily surface pressure. *Geophys. Res. Lett.,* **28,** 4114–4118.

——, and T. J. Dunkerton, 1999: Propagation of the Arctic Oscillation from the stratosphere to the troposphere. *J. Geophys. Res.,* **104,** 30 937–30 946.

——, and T. J. Dunkerton, 2001: Stratospheric harbingers of anomalous weather regimes. *Science,* **294,** 581–584.

Cash, B. A., P. J. Kushner, and G. K. Vallis, 2002: The structure and composition of the annular modes in an aquaplanet general circulation model. *J. Atmos. Sci.,* **59,** 3399–3414.

——, ——, and ——, 2004: Reply. *J. Atmos. Sci.,* **61,** 954–956.

——, ——, and ——, 2005: Zonal asymmetries, teleconnections, and annular patterns in a GCM. *J. Atmos. Sci.,* **62,** 207–219.

——, ——, and ——, 2007: Comment on "On the presence of annular variability in an aquaplanet model" by Masahiro Watanabe. *Geophys. Res. Lett.,* **34,** L03707, doi:10.1029/2006GL027274.

Chang, E. M. K., 1993: Downstream development of baroclinic waves as inferred from regression analysis. *J. Atmos. Sci.,* **50,** 2038–2053.

Cohen, J., and K. Saito, 2002: A test for annular modes. *J. Climate,* **15,** 2537–2546.

Deser, C., 2000: On the teleconnectivity of the Arctic Oscillation. *Geophys. Res. Lett.,* **27,** 779–782.

Franzke, C., S. Lee, and S. Feldstein, 2004: Is the North Atlantic Oscillation a breaking wave? *J. Atmos. Sci.,* **61,** 145–160.

Gerber, E. P., 2006: A dynamical and statistical understanding of the North Atlantic Oscillation and annular modes. Ph.D. thesis, Princeton University, 242 pp.

——, and G. Vallis, 2005: A stochastic model for the spatial structure of annular patterns of variability and the North Atlantic Oscillation. *J. Climate,* **18,** 2102–2118.

Gong, D., and S. Wang, 1999: Definition of Antarctic Oscillation index. *Geophys. Res. Lett.,* **26,** 459–462.

Hartmann, D. L., 1979: Baroclinic instability of realistic zonal-mean states to planetary waves. *J. Atmos. Sci.,* **36,** 2336–2349.

Hoskins, B. J., I. N. James, and G. H. White, 1983: The shape, propagation, and mean-flow interaction of large-scale weather systems. *J. Atmos. Sci.,* **40,** 1595–1612.

Limpasuvan, V., and D. L. Hartmann, 2000: Wave-maintained annular modes of climate variability. *J. Climate,* **13,** 4414–4429.

Lorenz, D. J., and D. L. Hartmann, 2001: Eddy–zonal flow feedback in the Southern Hemisphere. *J. Atmos. Sci.,* **58,** 3312–3327.

Rashid, H., and I. Simmonds, 2004: Eddy–zonal flow interactions associated with the Southern Hemisphere annular mode: Results from NCEP–DOE reanalysis and a quasi-linear model. *J. Atmos. Sci.,* **61,** 873–888.

Robinson, W. A., 2000: A baroclinic mechanism for the eddy feedback on the zonal index. *J. Atmos. Sci.,* **57,** 415–422.

——, 2004: Comments on "The structure and composition of the annular modes in an aquaplanet general circulation model." *J. Atmos. Sci.,* **61,** 949–953.

Simmons, A. J., and B. J. Hoskins, 1976: Baroclinic instability on the sphere: Normal modes of the primitive and quasi-geostrophic equations. *J. Atmos. Sci.,* **33,** 1454–1477.

Tanaka, H. L., and H. Tokinaga, 2002: Baroclinic instability in high latitudes induced by a polar vortex: A connection to the Arctic Oscillation. *J. Atmos. Sci.,* **59,** 69–82.

Thompson, D. W. J., and J. M. Wallace, 1998: The Arctic Oscillation signature in the wintertime geopotential height and temperature fields. *Geophys. Res. Lett.,* **25,** 1297–1300.

——, and ——, 2000: Annular modes in the extratropical circulation. Part I: Month-to-month variability. *J. Climate,* **13,** 1000–1016.

——, and S. Solomon, 2002: Interpretation of recent Southern Hemisphere climate change. *Science,* **296,** 895–899.

Vallis, G. K., E. P. Gerber, P. J. Kushner, and B. A. Cash, 2004: A mechanism and simple dynamical model of the North Atlantic Oscillation and annular modes. *J. Atmos. Sci.,* **61,** 264–280.

Wallace, J. M., 2000: North Atlantic Oscillation/Northern Hemisphere annular mode: One phenomenon, two paradigms. *Quart. J. Roy. Meteor. Soc.,* **126,** 791–805.

Watanabe, M., 2005: On the presence of annular variability in an aquaplanet model. *Geophys. Res. Lett.,* **32,** L05701, doi:10.1029/2004GL021869.